Research Article | Vol. 27, No. 13 | 24 Jun 2019 | OPTICS EXPRESS 18751

Optics EXPRESS

Two-dimensional symmetrical radial sub-aperture coherence and the local precision defect elimination method for high-precision beam steering

C. WANG,[1,2] Z. PENG,[1,2] Y. LIU,[1] S. LI,[1,2] Z. ZHAO,[1,2] W. CHEN,[1,2] Q. WANG,[1,3] AND Q. MU[1,2,4]

[1]*State Key Laboratory of Applied Optics, Changchun Institute of Optics, Fine Mechanics and Physics, Chinese Academy of Sciences, Changchun, 130033, China*
[2]*Center of Material Science and Optoelectronics Engineering, University of Chinese Academy of Sciences, Beijing, 100049, China*
[3]*qdwang@ciomp.ac.cn*
[4]*muquanquan@ciomp.ac.cn*

Abstract: Sub-aperture coherence (SAC) is a classical phase control method for high-precision beam steering using liquid crystal optical phased arrays (LCOPA). On this basis, radial sub-aperture coherence (RSAC) and symmetrical radial sub-aperture coherence (SRSAC) were proposed, which guarantee the stability of steering angles when the beam aperture and incident position fluctuate. In this article, the pre-existing one-dimensional SRSAC was firstly extended to a more universal 2D phase generation algorithm. Meanwhile, for the intractable problem of local precision defects caused by the basic two-dimensional variable period grating (2D-VPG) algorithm, we tracked their locations accurately and designed a targeted elimination method carefully. So these remarkable error peaks could be thoroughly removed by using 2D-SRSAC optimized by the local precision defect elimination method. Since then, all the excellent performance of 1D-SRSAC can be perfectly transplanted to 2D, which makes the non-mechanical beam steering technology using LCOPA more mature and competitive in the applications required ultra-high precision.

1. Introduction

Beam steering technology is widely used in many fields such as lidar [1,2] and free-space laser communication [3–5]. Since last century, the multitudinous non-mechanical beam steering techniques [6–9] have brought a new revolution in the field of photoelectric control, which realizes the agile beam scanning without inertia limitation and overcomes the main disadvantages of complex mechanical structure and high Size Weight and Power (SWaP) [10,11]. With the development of modern photoelectric system towards integration and portability, non-mechanical and high-precision beam steering technology represented by LCOPA [12,13] shows great potential especially in some specific applications such as optical acquisition, pointing and tracking (APT) of spatial dynamic objects [14,15].

In order to realize the beam steering with ultra-high angular resolution which cannot be realized by the primitive VPG algorithm, a series of sub-aperture segmentation methods were designed to improve the scanning accuracy [16] and ensure the stability of steering angle when the beam aperture error and the axis alignment error exist [17]. However, in order to achieve such an ultra-high precision in one dimension, the 2D pixel structure advantage of LCOPA, which could have been used to achieve 2D beam steering, was temporarily sacrificed in these new phase control algorithms. In fact, it can be verified that there is no necessary to abandon the steering ability in one direction when the ultra-high precision in the

#364796 https://doi.org/10.1364/OE.27.018751
Journal © 2019 Received 11 Apr 2019; revised 29 May 2019; accepted 29 May 2019; published 19 Jun 2019

Optics EXPRESS

other vertical direction is demanded, but the details of the algorithm need to be further optimized.

On the other hand, the extreme manifestation of uneven angular resolution in VPG is the existence of local precision defects, that is, the discrete error peaks. In recent years, some optimization methods to improve the VPG pointing accuracy have been proposed [18,19], in which the thorniest problem is that although the height of the error peaks can be reduced with the suppression of the overall pointing error, the loop optimization process of phase translation is probable to restrict the dynamic response speed of the beam steering system. Previous sub-aperture algorithms have been able to solve the problem of local precision defects to some extent without degrading the dynamic performance, but a small number of error peaks will still be neglected. For this reason, a new active method for straightforwardly eliminating the error peaks was designed to refine 2D-SRSAC so that these local precision defects can be thoroughly removed and the global ultra-high resolution can be finally realized in the agile beam scanning process.

In this article, the 2D steering strategy was extended directly by 1D-SRSAC and the related theory of local precision defects was firstly proposed. On this basis, the necessity of introducing local precision defect elimination method and its correction effect on steering angle arrays are verified by simulation. Finally, a steering angle measuring experiment with ultra-high precision was carried out to test the local beam steering performance of the ultimate optimized algorithm.

2. Theoretical analysis and relevant simulation

2.1 Conventional 2D-SRSAC algorithm

SRSRAC is essentially an angle interpolation process in which the sawtooth phase distribution corresponding to two endpoint angles are generated respectively in two sub-apertures and the fine-tuning of the steering angles between two endpoints can be implemented by adjusting the occupation rates of two sub-aperture areas. The principle and advantages of SRSAC for 1D beam steering has been detailedly introduced in [17], C. Wang et al. Technically, the advantages of ultra-high scanning accuracy and stability of 1D-SRSAC will be inherited if the phase surface is rotated at any azimuth. So 2D-SRSAC can be built on that basis, as shown in Fig. 1.

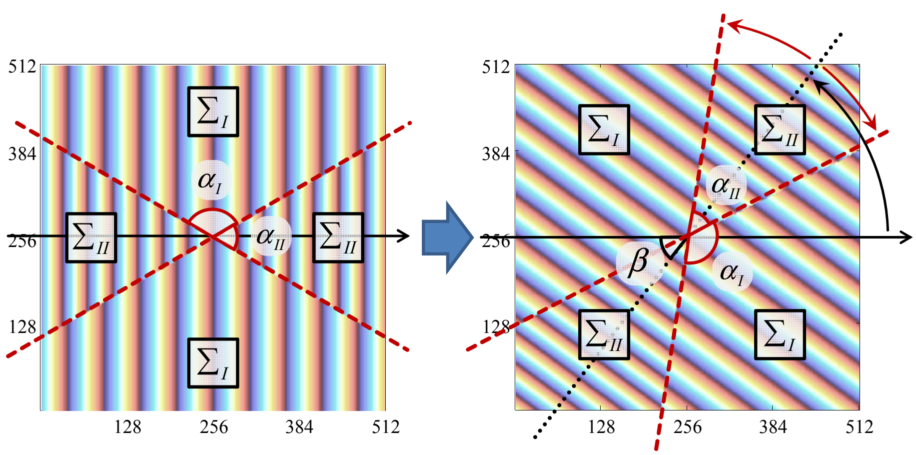

Fig. 1. A phase diagram for 2D steering derived from that for 1D steering.

For an arbitrary 2D steering angle $\boldsymbol{\theta} = (\theta_x, \theta_y)$, the corresponding 1D phase diagram is first generated according to the magnitude of the vector $\boldsymbol{\theta}$ and the whole phase function should be rotated by β, which represents the azimuthal angle of $\boldsymbol{\theta}$. α_I and α_{II} represent the sector angle of subdomains Σ_I and Σ_{II} respectively and vary from 0 to π to control the area occupation rates of two subdomains. The interpolation endpoint angles $\boldsymbol{\theta_I}$ and $\boldsymbol{\theta_{II}}$ corresponding to Σ_I and Σ_{II} are distributed on two concentric rings with a constant radius difference θ_{step}, so these two endpoint vectors are shown in Eq. (1), where the function *floor*() stands for rounding down and the function *angle*() stands for the vector azimuth.

$$\begin{aligned} &\left|\vec{\theta}_I\right| = \theta_{step} \cdot floor(\left|\vec{\theta}\right| / \theta_{step}), \left|\vec{\theta}_{II}\right| = \left|\vec{\theta}_I\right| + \theta_{step}, \\ &angle(\vec{\theta}_I) = angle(\vec{\theta}_{II}) = angle(\vec{\theta}) = \beta. \end{aligned} \tag{1}$$

Further, the normalized steering angle is redefined by Eq. (2) in the process of realizing desired angle $\boldsymbol{\theta}$ between the interpolation endpoints $\boldsymbol{\theta_I}$ and $\boldsymbol{\theta_{II}}$. At the same time, the simplified functional relationship between the occupation rate of the first subdomain ($\eta_I = \alpha_I / \pi$) and the normalized steering angle is given in Eq. (3) for the partition of sub-apertures, which is substantially the same as that in 1D steering.

$$\theta_{norm} \triangleq \frac{\left|\vec{\theta}\right| - \left|\vec{\theta}_I\right|}{\left|\vec{\theta}_{II}\right| - \left|\vec{\theta}_I\right|}. \tag{2}$$

$$\eta_I = (1 - \theta_{norm})^{2/5}. \tag{3}$$

On this basis, a series of equidistant scanning angles can be obtained by the accurate control of sub-aperture areas within specific interpolation segments, whose simulation diagram are shown in Fig. 2. Since the pixel structure on both sides of the vector $\boldsymbol{\theta}$ is no longer completely symmetric in the phase diagram with discrete coordinates, the actual scanning points in Fig. 2 may have some tolerable deviations perpendicular to $\boldsymbol{\theta}$, which has little effect on the overall performance of 2D-SRSAC.

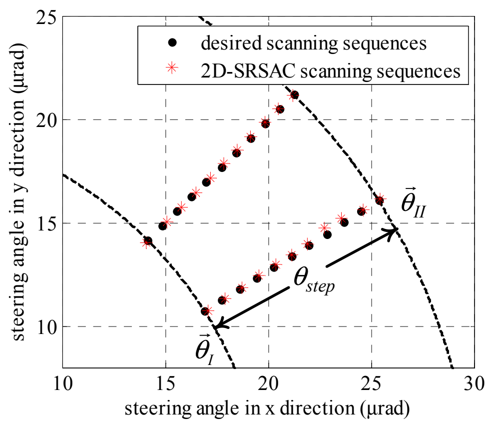

Fig. 2. Simulated diagram of equidistant scanning angle generation within scanning intervals.

The main advantage of this primary 2D algorithm is to greatly improve the resolution of the steering angles, ensure the stability and uniformity of that and slightly raise the pointing accuracy of the system. However, there is still plenty of scope for 2D-SRSAC to be optimized in terms of residual local precision defects

2.2 Property analysis of local precision defects

In the primitive 2D-VPG algorithm, the quantized phase modulated by actual LCOPAs leads to the generation of a large number of local precision defects in the whole beam steering range. In view of the fact that the pre-existing overall error suppression method may lead to

Research Article | Vol. 27, No. 13 | 24 Jun 2019 | OPTICS EXPRESS 18754

the degradation of the dynamic performance, a targeted method to snip out the error peaks straightforwardly must be adopted. Therefore, in order to design an optimized 2D-SRSAC algorithm which can realize this requirement faultlessly, the properties of these error peaks, such as their positions and widths, need to be firstly analyzed in detail. Taking 1D-VPG as a simplified example, a phase diagram used to demonstrate the origin of error peaks is shown in Fig. 3.

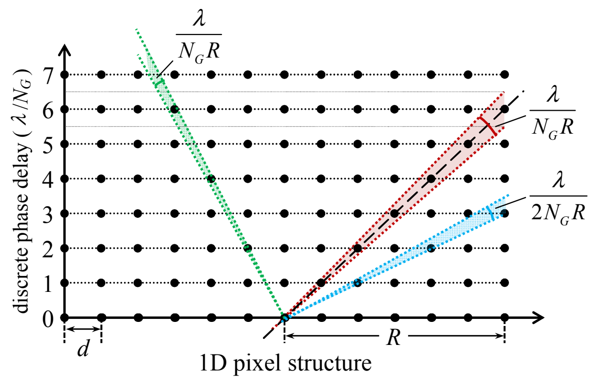

Fig. 3. The fragments of 1D tilted optical path delays. The red, green, and blue floating ranges correspond to the error peaks around the positions that the desired steering angles equal to $\lambda/N_G d$, $-2\lambda/N_G d$ and $\lambda/2N_G d$, respectively.

In Fig. 3, d is the pixel pitch, R is the effective radius of the incident light cross section, N_G is the number of quantized grayscale of the phase delay and λ is the wavelength of the modulated light, so λ/N_G is a minimum step of the optical path delays in the approximation of uniform grayscale. When the desired tilt fluctuates between the two red lines in Fig. 3, the output tilt must change to the fixed black dashed line because of the pixel-by-pixel rounding effect. Therefore, there will be a large pointing error in the neighborhood of this special angle, which is defined as θ_p in Eq. (4).

$$\theta_p = \frac{\lambda}{N_G \cdot d}. \tag{4}$$

Theoretically, the precision defect around θ_p contains two sub-peaks and the situation that the desired steering angle exactly equals to θ_p corresponds to the boundary point between them. Actually, they are so close to be regarded as one peak in the subsequent error elimination. The width of this main peak is defined as W_1 in Eq. (5), which is twice the floating angle of the tilt in Fig. 3 and felicitously describes the range size of this local precision defect.

$$W_1 = \frac{2\lambda}{N_G \cdot R}. \tag{5}$$

If the steering angle is redefined with the ratio of it to θ_p, that is, $m = \theta/\theta_p$, it is not difficult to find that when m is an arbitrary integer, there will be exactly a main error peak with the same peak width as shown in Eq. (5). The causes for these error peaks is the consistent rounding up or down of the phase values on all pixels when the ideal phase is approximate to the quantized phase. The floating tilt corresponding to another main error peak at $m = -2$ is shown by the green lines in Fig. 3. Furthermore, for an arbitrary fractional steering angle m in the steering range, if there is a minimum positive integer N such that N^*m is an integer, N will be defined as the order of the error peak at the steering angle m. Meanwhile, its peak width is defined as W_N in Eq. (6).

$$W_N = \frac{2\lambda}{N \cdot N_G \cdot R}. \tag{6}$$

The causes for these minor error peaks is the inerratic phase rounding with the period of $N*d$ and the floating tilt corresponding to 2-order minor error peak at $m = 1/2$ is shown by the blue lines in Fig. 3.

Although the phase gray distribution of actual devices is likely to deviate from the above assumption of isometric phase gray distribution, the phase calculation process still must be carried out in accordance with the equidistance grayscale generated by the ideal gamma correction, since then the property of the final error peak will remain basically unchanged. To verify the positions of the error peaks, the simulated diagram of the global steering error based on 1D-VPG has been made, as shown in Fig. 4.

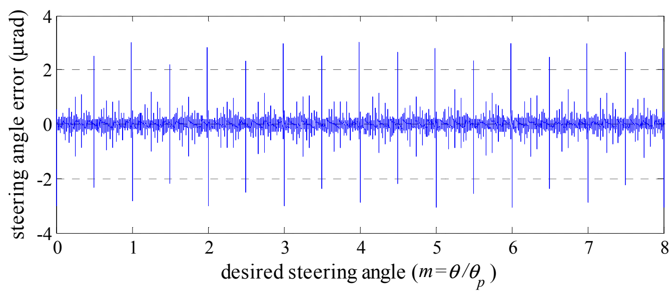

Fig. 4. Simulated diagram of the overall steering error based on 1D-VPG.

Mathematically, N-order minor error peaks can be defined at any rational steering angle m according to the previous analysis. Nevertheless, when N>4, the minor error peaks are so small and dense that they are entangled and treated as basic disturbances similar to white noise. So only the apparent error peaks whose order N are no more than 4 were analyzed and processed meticulously in the following work.

Refocus on the two-dimensional situation, N_x and N_y can be worked out in two directions independently by following the same definition in 1D case and the error peak will appear when both N_x*m_x and N_y*m_y are integers. But the final order N of 2D error peaks should be defined as the least common multiple of N_x and N_y for peak width calculation. The position and relative size diagram of error peaks whose orders $N≤4$ in the square area $[0, 1]^2$ is shown in Fig. 5, where the color of the error peaks approximately represents the peak height, that is, the estimated value of the error size. Meanwhile, the error peak distribution in the whole two-dimensional coordinate plane takes the sub-distribution in this square area as the minimum repetition period.

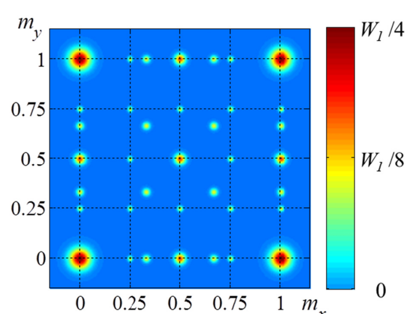

Fig. 5. Position and relative size diagram of the error peaks in $[0, 1]^2$ based on 2D-VPG.

Optics EXPRESS

Considering that the error peaks with different positions but the same orders N have almost the same width and height, we respectively select one error peak from the peaks with different order N for simulation verification. The simulation parameters are selected according to the actual experimental system, where λ = 730nm, R = 3000mm, N_G = 40 and d = 15μm. Figure 6 is the simulated result of the error peaks with different order N, which verified the rationality of Eqs. (4)-(6). It is important to note that the so-called "error at a point" in Fig. 6 actually refers to the error in the neighborhood of the point, regardless of main error peaks or higher order minor peaks.

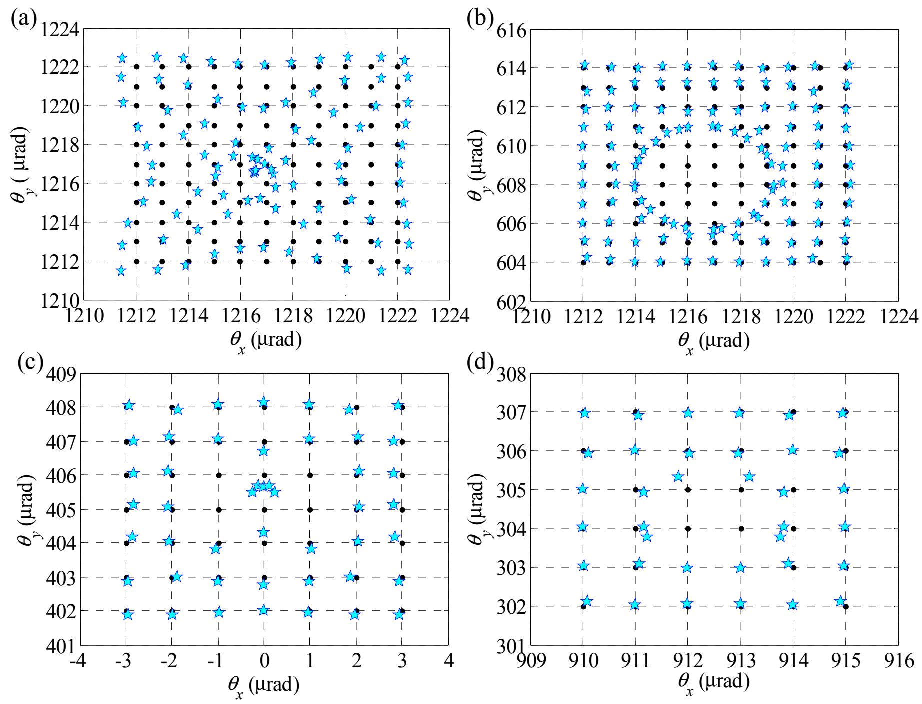

Fig. 6. Simulated diagram of error peaks based on 2D-VPG. (a) The main error peak for N = 1 and (m_x , m_y) = (1,1). (b) The minor error peak for N = 2 and (m_x , m_y) = (1,1/2). (c) The minor error peak for N = 3 and (m_x , m_y) = (0,1/3). (d) The minor error peak for N = 4 and (m_x , m_y) = (3/4,1/4).

2.3 The ultimate elimination method of local precision defects

In the previous section, the causes and properties of local precision defects based on VPG have been introduced in detail. Technically, the thought of steering angle interpolation can make the fluctuation of pointing error tend to be smooth, so initial SRSAC already has elimination effect for local error peaks no matter in 1D or 2D cases, but this capability can be ulteriorly optimized. Still taking 1D beam steering as an example, the global steering error based on conventional SRSAC is shown in Fig. 7. Compared with Fig. 4, it can be found that most of the error peaks have been completely removed. However, a small number of error peaks still escape the elimination successfully, which needs to be further resolved in applications where the quantity limitation of noise points is particularly stringent.

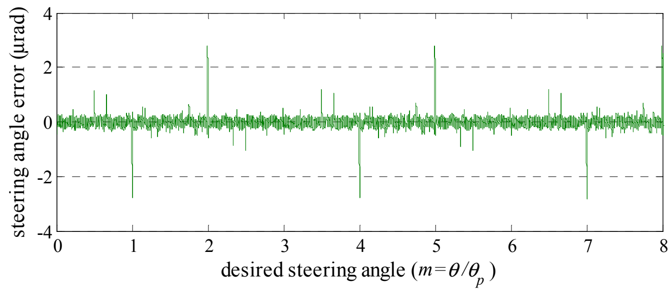

Fig. 7. Simulated diagram of the overall steering error based on conventional 1D-SRSAC.

The reason for such imperfections is obvious. In conventional SRSAC, the selection of interpolation endpoints can never be adjusted according to the neighboring VPG pointing accuracy. Therefore, when an endpoint used for interpolation happens to be within an error peak, it will drive the pointing error in the neighborhood to increase dramatically in the same direction and that is why there are a small number of unilateral peaks in Fig. 7 that have not been successfully removed.

Since the position and the range of these precision defects have been clearly estimated in section 2.2, the positions of interpolation endpoints can be adjusted actively. Considering that the larger θ_{step} , the worse interpolation precision, the initial value of θ_{step} in conventional SRSAC is set to approximately equal to the range diameter of main error peaks so that the situation where both two endpoints fall into one error peak can be furthest avoided. However, the endpoint positions in the active local precision defect elimination method are required to be stricter. In order to ensure that either of two endpoints does not fall into one error peak, the value of $|\boldsymbol{\theta_{II}} - \boldsymbol{\theta_I}|$ firstly has to be doubled to $2\theta_{step}$. Since then, the midpoint $(\boldsymbol{\theta_I} + \boldsymbol{\theta_{II}})/2$ and any endpoints of a interpolation segment can no longer be affected at the same time by one error peak. On this basis, if either of the two endpoints calculated by Eq. (1) is within an error peak, the entire interpolation segment needs to move up or down the length of θ_{step} in the radial direction, as shown in Fig. 8.

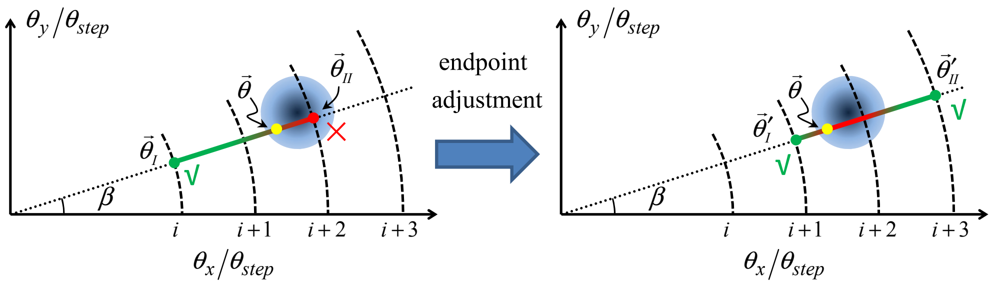

Fig. 8. Schematic diagram of the interpolation segment adjustment in the local error elimination process.

In Fig. 8, the blue circle represents an error peak which contains an endpoint auto-generated by the primary 2D-SRSAC. After the interpolation segments are adjusted, any endpoints are ensured to be outside the error peak so that the quondam bad points can be replaced smoothly by the linear interpolation points. More specifically, if the distance from any one of the endpoints to the center of an arbitrary error peak is less than its half width as well as $|\boldsymbol{\theta_I}| \neq 0$, the magnitude of the endpoints needs to be changed to Eq. (7). Meanwhile, the normalized steering angle θ_{norm} needs to be recalculated by Eq. (2) based on the location of the new endpoints.

$$\left|\vec{\theta}_I\right| = 2\theta_{step} \cdot floor\left[\left(\left|\vec{\theta}\right| - \theta_{step}\right)/2\theta_{step}\right] + \theta_{step}, \left|\vec{\theta}_{II}\right| = \left|\vec{\theta}_I\right| + 2\theta_{step}. \tag{7}$$

After doubling the interpolation segment length and adjusting the endpoint locations according to the properties of error peaks, the suppression effect of the local precision defects can be obtained from the global simulation of 1D steering error, as shown in Fig. 9.

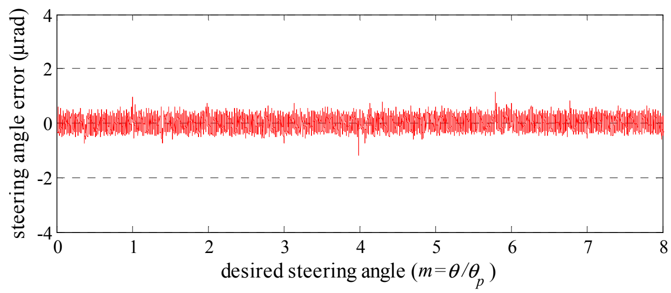

Fig. 9. Simulated diagram of the overall steering error based on the optimized 1D-SRSAC.

From Fig. 9, it can be seen that all the error peaks have been completely eliminated as expected. However, the shortcomings of this method are also visible, that is, the enhancement of the basic error fluctuation compared to Figs. 4 and 7. The most intuitive reason for this deficiency is the longer interpolation segment, in which case the error of linear interpolation based on Eq. (3) will inevitably increase.

In addition, even assuming perfect interpolation, a steering angle can also be affected by the error of its two adjacent endpoints. Ignoring a few bad points in the error peak, it can be concluded from a statistical perspective that the interpolation endpoints based on 2D-VPG follow 2D normal distribution $N(E(\boldsymbol{\theta}),\sigma^2)$ in the overall steering range. On this basis, it can be proved that the deviations of internal interpolated points are also normally distributed and their mathematical expectation and variance can be worked out, as shown in Eqs. (8) and (9) respectively.

$$E(\vec{\theta}) = \theta_{norm} \cdot E(\vec{\theta}_{II}) + (1-\theta_{norm}) \cdot E(\vec{\theta}_I), \tag{8}$$

$$\mathrm{var}(\vec{\theta}) = [1-(2\theta_{norm} - 2\theta_{norm}{}^2)(1-c)]\sigma^2, c = [E(\vec{\theta}_I \cdot \vec{\theta}_{II}) - E(\vec{\theta}_I) \cdot E(\vec{\theta}_{II})]/\sigma^2. \tag{9}$$

In Eq. (9), the parameter c stands for the correlation coefficient of two endpoints and is determined only by the interpolation segment length θ_{step} = $|\boldsymbol{\theta_{II}}$ -$\boldsymbol{\theta_I}$ |. By utilizing the simulated data in Fig. 4, the relationship between them can be obtained, as shown in Fig. 10, in which the correlation coefficient decays when the interpolation segment length is only a few micro-radians but then oscillates periodically.

Optics EXPRESS

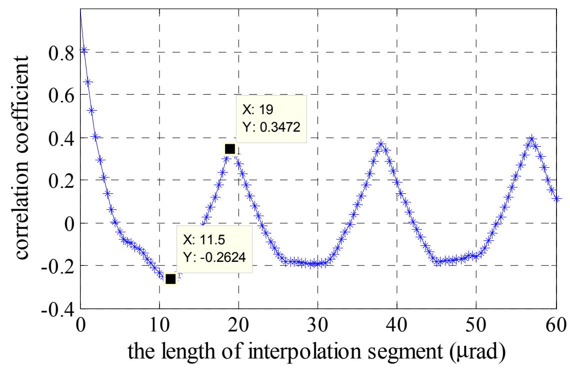

Fig. 10. The relationship between correlation coefficient and the interpolation segment length.

Obviously, it can be seen from Eq. (9) that the smaller correlation coefficient results in smaller fluctuation of the interpolate angle error. Therefore, to reduce the global steering error, the most suitable interpolation segment length should be selected around 10μrad rather than 20μrad according to Fig. 10, which is another essential reason for the overall precision deterioration in Fig. 9.

In general, the interpolation segment length can determine not only the accuracy of the interpolation process itself, but also the influence of the endpoint fluctuation on the output angle. Taking these two factors into consideration, it is necessary to set variable interpolation segment length to balance the contradiction between the elimination effect of local error peaks and the average amplitude of global deviation. Since the positions of error peaks have been known, we can double the interpolation segment length to $2\theta_{step}$ only near error peaks, but still adopt θ_{step} in the steering range other than error peaks. The 1D global steering error distribution based on the ultimate precision defect elimination method will combine the advantages of Figs. 7 and 9. Meanwhile, the correction effect of the local error peaks is shown in Fig. 11.

Optics EXPRESS

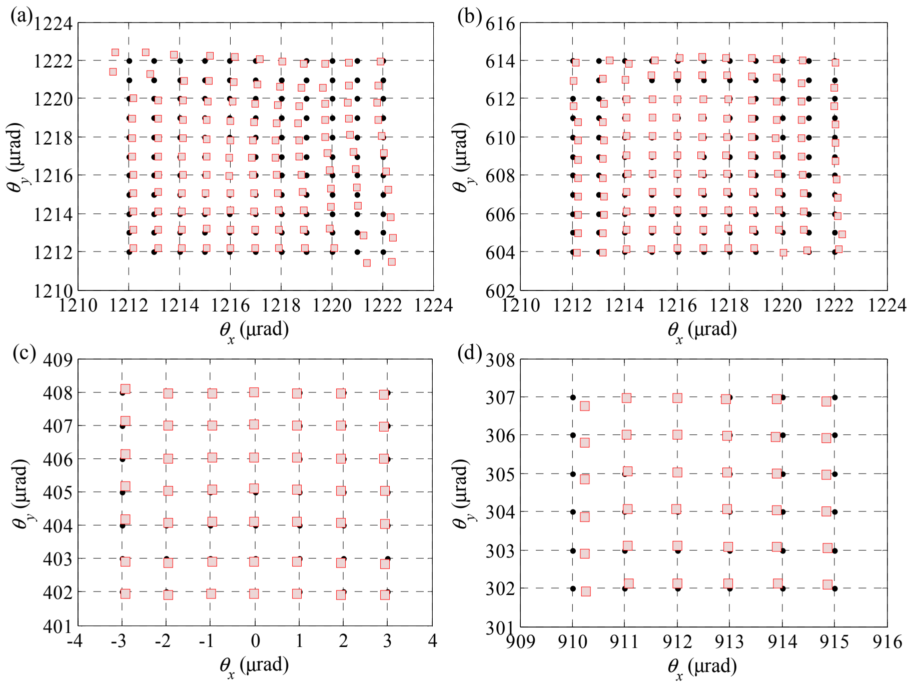

Fig. 11. Simulated diagram of the correction effect of error peaks based on 2D-SRSAC optimized by the precision defect elimination method. (a) The main error peak for $N = 1$ and $(m_x , m_y) = (1,1)$. (b) The minor error peak for $N = 2$ and $(m_x , m_y) = (1,1/2)$. (c) The minor error peak for $N = 3$ and $(m_x , m_y) = (0,1/3)$. (d) The minor error peak for $N = 4$ and $(m_x , m_y) = (3/4,1/4)$.

Compared with Fig. 5, it can be seen that the modified 2D-SRSAC has a pretty conspicuous correction effect of local precision defects and the residual traces of minor error peaks can hardly be seen. A small amount of systematic error appears in Fig. 11(a) but its magnitude has been reduced to the same level as the basic overall fluctuation, which is within an acceptable range.

3. Verification experiment

After the optimized 2D-SRSAC has been proved to be available from simulation, a high precision measuring setup for 2D steering angles was carefully built to further verify its actual performance of local error suppression. Figures. 12 and 13 are the schematic diagram and physical photo of the 2D steering angle measuring setup with corresponding phase distribution instances, respectively.

Optics EXPRESS

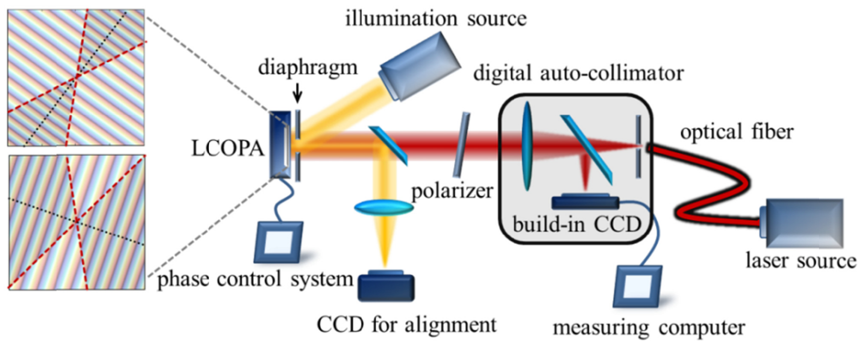

Fig. 12. Schematic diagram of the 2D steering angle measuring setup and phase distributions.

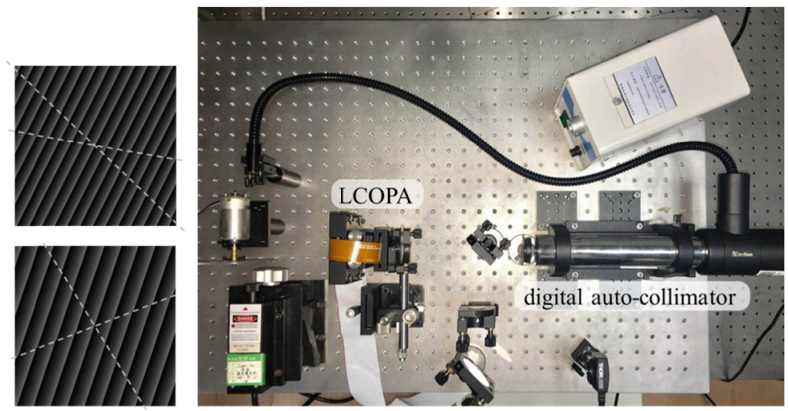

Fig. 13. Physical diagram of the 2D steering angle measuring setup and the actual phase driving instructions, where the difference of stripe widths in two sub-apertures has been exaggerated in Fig. 12.

The measuring setup is mainly composed of LCOPA, digital auto-collimator and oblique illuminating system. The digital auto-collimator first emits collimated beams that have eliminated the speckle effect, then receives the light reflected by the modulator panel and works out the steering angle basing on the spot position focused on the built-in CCD. The oblique illuminating system is introduced to facilitate the accurate alignment of the adjustable diaphragm and the panel center of LCOPA. The wavelength of the incident light is 730nm, the aperture is 6mm, the pixel pitch of LCOPA is 15μm, the optimal gray level after gamma correction is 40 and the initial interpolation segment length (θ_{step}) in 2D-SRSAC is set to 10μrad. The initial steering angle data can be obtained in the measuring interface of the auto-collimator, as shown in Fig. 14. The data at the upper-left corner of each sub-graph represent the incident angle of the beam when the panel of LCOPA is equivalent to a mirror.

Optics EXPRESS

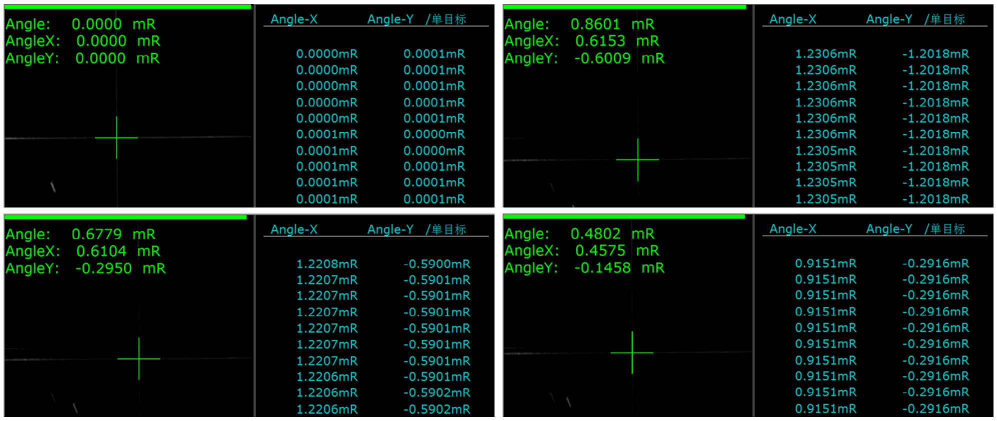

Fig. 14. The measuring interface with the steering angles at the zero point and around different positions of error peaks.

After the known system error of the measuring instrument has been removed, the actual steering angle arrays within the neighborhood of error peaks based on 2D-VPG and optimized 2D-SRSAC are measured respectively, as shown in Figs. 15 and 16.

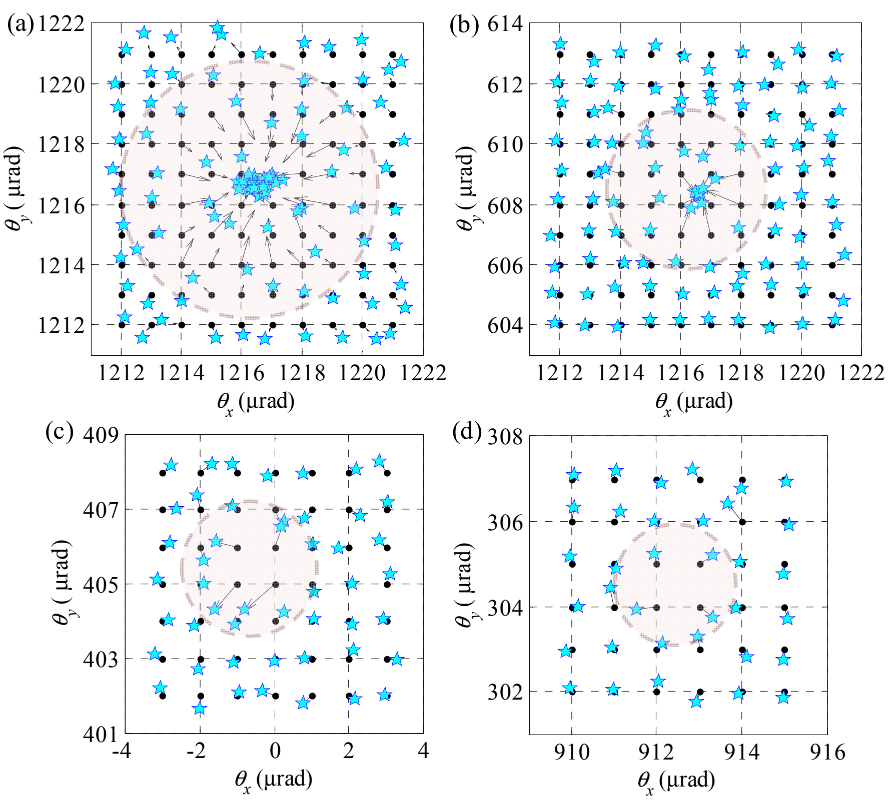

Fig. 15. Measured data of error peaks based on the primitive 2D-VPG algorithm. (a) The main error peak for $N = 1$ and $(m_x , m_y) = (1,1)$. (b) The minor error peak for $N = 2$ and $(m_x , m_y) = (1,1/2)$. (c) The minor error peak for $N = 3$ and $(m_x , m_y) = (0,1/3)$. (d) The minor error peak for $N = 4$ and $(m_x , m_y) = (3/4,1/4)$.

The test results of the steering angles based on 2D-VPG have adequately confirmed the theoretical prediction about the positions and widths of error peaks. Although the convergence trend of the steering angle array in Fig. 15(b) does not fully coincide with the divergent trend of the simulated data in Fig. 6(b), it does not affect the judgment on the position and width of the error peak. In addition, the identifiability of the 4-order error peak shown in Fig. 15(d) has decreased apparently, which proves that it is reasonable to just eliminate the error peaks whose orders are no more than 4. The error peaks with higher order were also tested tentatively, but their widths are so small that they are completely beyond the identification ability of our measuring instrument and lost the significance of being carefully corrected.

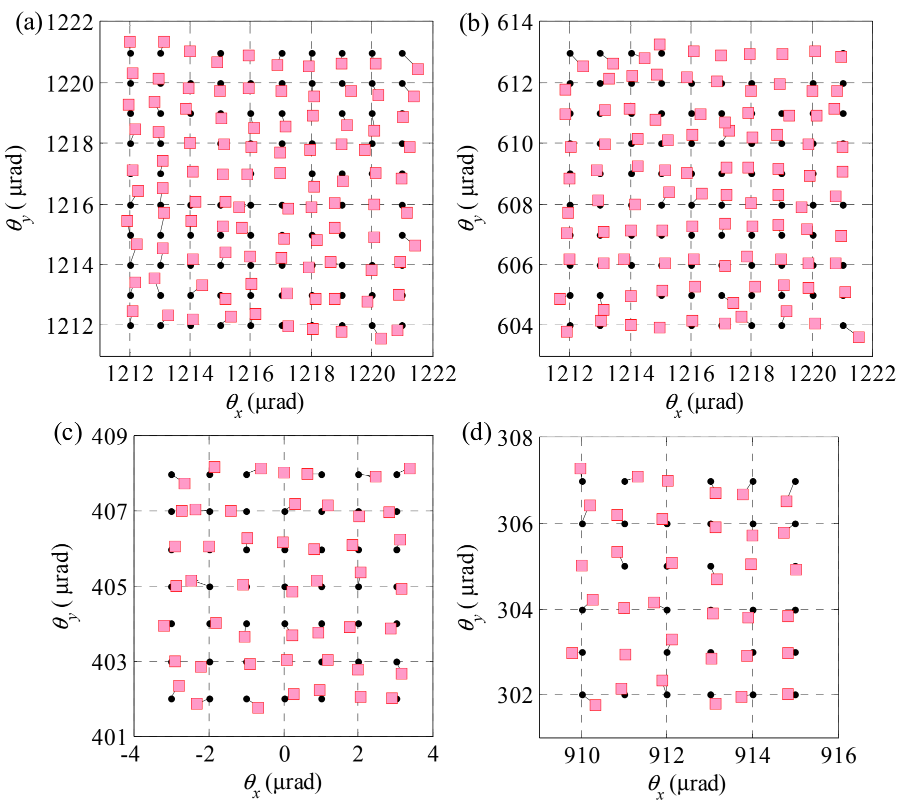

Fig. 16. Measured data of error peaks with different order N based on the optimized 2D-SRSAC algorithm. (a) The main error peak for $N = 1$ and $(m_x, m_y) = (1,1)$. (b) The minor error peak for $N = 2$ and $(m_x, m_y) = (1,1/2)$. (c) The minor error peak for $N = 3$ and $(m_x, m_y) = (0,1/3)$. (d) The minor error peak for $N = 4$ and $(m_x, m_y) = (3/4,1/4)$.

Compared with the primitive 2D-VPG algorithm, the optimized 2D-SRSAC has conspicuous correction effect especially at the positions of the error peaks whose order are 1 or 2. In order to quantitatively compare the deviations between the actual steering angle arrays and the ideal cases, the error RMS of two algorithms in different positions have been further counted in Table 1.

Table 1. RMS of steering angle error at different position (μrad)

(m_x, m_y)	(1, 1)	(1, 1/2)	(0, 1/3)	(3/4, 1/4)
2D-VPG	1.20	0.36	0.34	0.27
2D-SRSAC	0.35	0.27	0.28	0.27

As can be seen from Table 1, the error elimination ability of the optimized 2D-SRSAC is undeniable, which would be more obvious in terms of RMS data if the random measuring errors could be removed. Except for a little residual systematic error around the position of $(m_x, m_y) = (1,1)$, the RMS of the steering angle arrays generated by the optimized 2D-SRSAC are at the same level, which indicates that the minor error peaks of 2D-VPG have been completely eliminated, even if their accuracy advantage over the VPG steering points has not been highlighted due to the doubling of the local interpolation segment length. As predicted by the simulated results in Fig. 11(a), a small number of acceptable blemishes near the main error peak appeared in Fig. 16(a) becauseθ_{step} cannot be set large enough to completely avoid the influence of the error peak sidelobes when the global error suppression is taken into account.

On the other hand, in order to verify the effectiveness of the local precision defect elimination method, the measured steering angle ranges are carefully considered rather than randomly selected especially for main error peaks and 2-order error peaks which are easier to be identified. The steering angles were measured at $(m_x, m_y) = (1, 1)$ and $(1, 1/2)$ to represent the deviation of steering angles in the vicinity of main error peaks and 2-order error peaks respectively. Thus their corresponding magnitudes are $\sqrt{2}\,\theta_p$ and $\sqrt{5}\,\theta_p/2$, which are very close to the integer times of θ_{step}. Such a situation means that the distances between some default interpolation endpoints of conventional 2D-SRSAC and the error peak centers will be distinctly less than the half widths of the corresponding error peaks, which makes the steering angles generated by these endpoints severely affected by the error peaks. Fortunately, with our local precision defect elimination method, the interpolation segment length near error peaks will be doubled to $2\theta_{step}$ and the endpoint positions will be actively adjusted to avoid the areas covered by the error peaks. Finally, there is almost no apparent systematic error of the steering angle arrays in Figs. 16(a) and 16(b), which indicated that the local precision defect elimination method has a great optimization effect on 2D-SRSAC.

4. Conclusion

In this paper, we firstly extend the one-dimensional SRSAC to two-dimension and retained the essential advantages of this phase generation methods. More importantly, the local precision defects caused by primitive 2D-VPG are analyzed in detail and the main parameters of these error peaks such as the position and width are explicitly presented. On this basis, the local precision defect elimination method for optimizing 2D-SRSAC has been designed so that the steering angle near the error peaks can thoroughly avoid their disturbance by doubling the interpolation segment length and actively adjusting the positions of interpolation endpoints. Finally, an impeccable phase generation scheme for 2D beam steering with ultra-high resolution, no local precision defects is determined, which ensures the 2D non-mechanical dynamic beam steering system has more prominent and reliable performance in the applications with extremely high precision requirement.

Funding

National Natural Science Foundation of China (11604327, 11704377, 11804336, 61405194, 11774342, 61805238, 61475152, 61775212, 61811530061, 61378075 and 61377032) and Department of Science and Technology of Jilin Province (20170519016JH).

Optics EXPRESS

Acknowledgments

This work was supported by the National Natural Science Foundation of China and CAS Interdisciplinary Innovation Team.

References

1. S. Davis, S. D. Rommel, D. Gann, B. Luey, J. D. Gamble, M. Ziemkiewicz, and M. Anderson, “A lightweight, rugged, solid state laser radar system enabled by non-mechanical electro-optic beam steerers,” Proc. SPIE **9832**, 98320K (2016).
2. N. L. Seldomridge, J. A. Shaw, and K. S. Repasky, “Dual-polarization lidar using a liquid crystal variable retarder,” Opt. Eng. **45**(10), 106202 (2006).
3. Y. Lin, M. Mahajan, D. Taber, B. Wen, and B. Winker, “Compact 4 cm aperture transmissive liquid crystal optical phased array for free-space optical communications,” Proc. SPIE **5892**, 58920C (2005).
4. B. Winker, M. Mahajan, and M. Hunwardsen, “Liquid crystal beam directors for airborne free-space optical communications,” in Proceedings of IEEE Aerospace Conference (IEEE, 2004), Vol.**3**, pp. 1702–1709.
5. W. J. Miniscalco and S. A. Lane, “Optical space-time division multiple access,” J. Lightwave Technol. **30**(11), 1771–1785 (2012).
6. D. Winick, B. Duewer, S. Chaudhury, J. Wilson, J. Tucker, U. Eksi, and P. Franzon, “MEMS-based diffractive optical-beam-steering technology,” Proc. SPIE **3276**, 81–87 (1998).
7. J. Kim, C. Oh, M. J. Escuti, L. Hosting, and S. Serati, “Wide-angle, nonmechanical beam steering using thin liquid crystal polarization gratings,” Proc. SPIE **7093**, 709302 (2008).
8. E. A. Watson, W. E. Whitaker, C. D. Brewer, and S. R. Harris, “Implementing optical phased array beam steering with cascaded microlens arrays,” in Proceedings of IEEE Aerospace Conference (IEEE,) **3**, 1429–1436 (2002).
9. N. R. Smith, D. C. Abeysinghe, J. W. Haus, and J. Heikenfeld, “Agile wide-angle beam steering with electrowetting microprisms,” Opt. Express **14**(14), 6557–6563 (2006).
10. P. F. McManamon, T. A. Dorschner, D. L. Corkum, and L. J. Friedman, “Optical phased array technology,” in Proceedings of IEEE (IEEE,), **84**(2), 268–298 (1996).
11. P. F. Mcmanamon, P. J. Bos, M. J. Escuti, J. Heikenfeld, S. Serati, H. Xie, and E. A. Watson, “A review of phased array steering for narrow-band electrooptical eystems,” in Proceedings of IEEE (IEEE), **97**(6), 1078–1096 (2009).
12. Z. Zhang, Z. You, and D. Chu, “Fundamentals of phase-only liquid crystal on silicon (LCOS) devices,” Light Sci. Appl. **3**(10), e213 (2014).
13. D. Vettese, “Liquid crystal on silicon,” Nat. Photonics **4**(11), 752–754 (2010).
14. X. Wang, J. Xu, Z. Huang, W. Liang, T. Zhang, S. Wu, and Q. Qi, “Theoretical model and experimental verification on the PID tracking method using liquid crystal optical phased array,” Proc. SPIE **10096**, 1009618 (2017).
15. E. Haellstig, J. Stigwall, M. Lindgren, and L. Sjoqvist, “Laser beam steering and tracking using a liquid crystal spatial light modulator,” Proc. SPIE **5087**, 13–23 (2003).
16. Z. Tang, X. Wang, Z. Huang, Q. Tan, Y. Duan, G. Suo, J. Du, and Q. Qiu, “Sub-aperture coherence method to realize ultra-high resolution laser beam deflection,” Opt. Commun. **335**, 1–6 (2015).
17. C. Wang, Z. Peng, Y. Liu, S. Li, Z. Zhao, W. Chen, Q. Wang, and Q. Mu, “Radial sub-aperture coherence method used to achieve beam steering with high precision and stability,” Opt. Express **27**(5), 6331–6347 (2019).
18. D. Engström, J. Bengtsson, E. Eriksson, and M. Goksör, “Improved beam steering accuracy of a single beam with a 1D phase-only spatial light modulator,” Opt. Express **16**(22), 18275–18287 (2008).
19. L. Kong, Y. Zhu, Y. Song, and J. Yang, “Beam steering approach for high-precision spatial light modulators,” Chin. Opt. Lett. **8**(11), 1085–1089 (2010).